Size dependence of photocatalytic oxidation reactions of Rh nanoparticles dispersed on (Ga1-xZnx)(N1-xOx) support

Document Version:

Publisher's PDF, also known as Version of Record (includes final page, issue and volume numbers)

Please check the document version of this publication:

• A submitted manuscript is the version of the article upon submission and before peer-review. There can be important differences between the submitted version and the official published version of record. People interested in the research are advised to contact the author for the final version of the publication, or visit the DOI to the publisher's website.
• The final author version and the galley proof are versions of the publication after peer review.
• The final published version features the final layout of the paper including the volume, issue and page numbers.

Link to publication

Article

Size dependence of photocatalytic oxidation reactions of Rh nanoparticles dispersed on (Ga1-xZnx)(N1-xOx) support

Yi Zhang, D. A. J. Michel Ligthart, Peng Liu, Lu Gao, Tiny M. W. G. M. Verhoeven, Emiel J. M. Hensen *

Department of Chemical Engineering and Chemistry, Eindhoven University of Technology, P.O. Box 513, 5600 MB, Eindhoven, The Netherlands

ARTICLE INFO

ABSTRACT

Mixed Ga–Zn oxynitrides were synthesized using coprecipitation, wet-precipitation, and solid-solution methods. The oxynitrides were used as supports for Rh nanoparticle catalysts in photocatalytic water splitting, CO oxidation, and H_2 oxidation. Mixed Ga–Zn oxynitrides produced by wet precipitation and nitridation had good visible-light-absorption properties and high surface areas, so they were used to support uniformly sized poly(vinylpyrrolidone)-stabilized Rh nanoparticles. The nanoparticle size range was 2–9 nm. These catalysts had negligible activity in photocatalytic H_2 production by water splitting with methanol as a sacrificial agent. Other mixed Ga–Zn oxynitrides were also inactive. A reference sample provided by Domen also showed very low activity. The influence of particle size on Rh-catalyzed oxidation of CO and H_2 was investigated. For CO oxidation, the activities of small particles were higher for particles with higher Rh oxidation degrees. The opposite holds for H_2 oxidation.

1. Introduction

Among the many systems explored for photocatalytic water splitting, mixed Ga–Zn oxynitrides $(Ga_{1-x}Zn_x)(N_{1-x}O_x)$ modified with Cr_2O_3-encapsulated noble metal cocatalysts constitute a promising and attractive catalyst system [1–3]. Maeda et al. [1–3] were the first to report the good performance of $(Ga_{1-x}Zn_x)(N_{1-x}O_x)$ solid solutions as light-harvesting semiconductors for water splitting under visible-light irradiation. $(Ga_{1-x}Zn_x)(N_{1-x}O_x)$ samples were synthesized by mixing Ga_2O_3 and ZnO powders, followed by heating in NH_3 (nitridation) [1]. The resulting solid solution has a narrow band gap (2.4–2.8 eV) compared with those of GaN (3.4 eV) and ZnO (3.2 eV) reference materials. The same authors later performed a series of investigations into the influence of the starting materials, nitridation conditions, and post-calcination treatment on the photocatalytic activity. The crystallinity and composition of $(Ga_{1-x}Zn_x)(N_{1-x}O_x)$ are important factors for achieving good cat-

alytic performance [2,4–10]. However, the solid-state reaction is laborious and results in a low surface area (<10 m^2/g), bulk defects, and a low ZnO content [11–13]. Moriya et al. [14] suggested that the Zn content of $(Ga_{1-x}Zn_x)(N_{1-x}O_x)$ could not exceed $x = 0.4$ because Zn^{2+} is easily reduced to Zn metal, which evaporates at high temperatures in reducing atmospheres. This limits the visible-light absorption of the prepared solids. Consistent with this, an increase in the Zn content of the crystalline structure results in a shift of the absorption edge to higher wavelengths [15–18]. Han et al. [16] used a sol-gel method to synthesize $(Ga_{1-x}Zn_x)(N_{1-x}O_x)$ ($x = 0.482$) with the absorption edge at 560 nm. Lee et al. [17] synthesized $(Ga_{1-x}Zn_x)(N_{1-x}O_x)$ by nitridation of a mixture of $ZnGa_2O_4$ and ZnO nanocrystals to tune the Zn content from $x = 0.30$ to 0.87, giving absorption-edge values ranging from 460 to 565 nm. Li et al. [19] also prepared $(Ga_{1-x}Zn_x)(N_{1-x}O_x)$ by the method used by Lee et al. [17], but used $ZnGa_2O_4$ and ZnO nanofibers to obtain nanostructured $(Ga_{1-x}Zn_x)(N_{1-x}O_x)$ with a high surface area and

high Zn ratio (x = 0.5) by nitriding at 650 °C. It is therefore desirable to develop novel and more facile methods for low-temperature synthesis of $(Ga_{1-x}Zn_x)(N_{1-x}O_x)$ materials with improved photocatalytic activities.

Recently, soft chemical methods for preparing $(Ga_{1-x}Zn_x)$-$(N_{1-x}O_x)$ from layered double hydroxide (LDH) precursors have been explored [20,21]. Materials derived from LDHs have large surface areas (100–300 m²/g) [20]. Zou et al. [13] reported the synthesis of $(Ga_{1-x}Zn_x)(N_{1-x}O_x)$ from a $ZnGa_2O_4$ precursor by nitridation to obtain products with higher Zn and lower N contents, and larger surface areas than those of the original materials reported by the Domen group. Such $ZnGa_2O_4$ phosphors with spinel structures were obtained by calcining single-phase Zn_3Ga-based LDHs of relatively small size. However, this route is less facile because it requires two calcination steps from LDHs to $(Ga_{1-x}Zn_x)(N_{1-x}O_x)$. Wang et al. [21] used a simple method based on direct nitridation of LDHs containing Zn^{2+}, Ga^{3+}, and $CO_3{}^{2-}$. Compared with the conventional solid-solution method involving nitridation for 15 h, this synthetic method requires a shorter nitridation time (0.5 h). Zn-rich $(Ga_{1-x}Zn_x)$-$(N_{1-x}O_x)$ can be obtained because Zn is stabilized in the interlayer region of the LDH precursors [20]. Mapa et al. [22] reported a simple synthesis of $(Ga_{1-x}Zn_x)(N_{1-x}O_x)$ by fast combustion of aqueous solutions of $Ga(NO_3)_3$ and $Zn(NO_3)_2$ with urea in a furnace at 500 °C.

$(Ga_{1-x}Zn_x)(N_{1-x}O_x)$ materials do not show photocatalytic activities without cocatalysts. It was found that Rh/Cr_2O_3 core–shell structures are the best cocatalysts for H_2 production. The Domen group investigated the effect of the size of Rh particles supported on $(Ga_{1-x}Zn_x)(N_{1-x}O_x)$; they compared photodeposition, impregnation, and adsorption as methods for introducing Rh and also explored the promoting effect of Cr_2O_3. Rh nanoparticle (NP) dispersion was found to be important for the rate of H_2 production; this was attributed to the need for a high Rh surface area [23]. Ikeda et al. [24] reported that poly(vinylpyrrolidone) (PVP)-stabilized Rh NPs can act as highly dispersed cocatalysts on semiconductors. Our recent work shows that the Rh NP density is more important than the particle size because a high rate of removal of charge carriers from the semiconductor is important [27]. It is worth mentioning that smaller supported Rh particles are more prone to oxidation than larger ones [25,26].

In the present study, we considered that it would be valuable to study the relation between the preparation methods, structures, and catalytic activities of $(Ga_{1-x}Zn_x)(N_{1-x}O_x)$ materials systematically. Based on our earlier work [27], we were also interested in investigating the influence of the Rh cocatalyst NP size on the oxidation states of Rh NPs, using extended X-ray absorption fine-structure (EXAFS) and X-ray absorption near-edge structure (XANES) methods, and the rate of photocatalytic H_2 production by water splitting. We also evaluated these catalysts for the oxidation of CO and H_2 to understand the influence of NP size and oxidation state on these elementary reactions.

2. Experimental

2.1. Synthesis of $(Ga_{1-x}Zn_x)(N_{1-x}O_x)$

Mixed zinc oxide/gallium nitrides were synthesized using the methods reported in the literature [1,13,21]. For coprecipitation (samples denoted by "C"), $Zn(NO_3)_2\cdot6H_2O$ (≥99.0%, Sigma-Aldrich; 11.9 g) and $Ga(NO_3)_3\cdot xH_2O$ (99.9%, Alfa Aesar; 6.6 g) were dissolved in deionized water (60 mL; solution A), NaOH (≥97%, Merck; 4.8 g) in deionized water (60 mL; 2 mol/L NaOH, solution B), and Na_2CO_3 (anhydrous, Merck; 3.2 g) in deionized water (60 mL; 0.03 mol/L Na_2CO_3, solution C). Solutions A and B were added dropwise to solution C while controlling the pH at 10. The mixture was stirred and aged for 20 h at 65 °C in a water bath. The suspension was filtered, and the obtained powder was dried at 110 °C for 12 h and calcined in a 20% O_2/He flow at 900 °C (5 °C/min) for 6 h. The calcined material was transferred to a 10 mol/L NaOH solution and stirred at 65 °C for 20 h, followed by filtering and washing with deionized water. It was then dried overnight to form $ZnGa_2O_4$ spinel. The $ZnGa_2O_4$ spinel powder was heated at temperatures in the range 500–900 °C in a pure NH_3 flow (200 mL/min) for 10 h.

The wet-precipitation method (samples denoted by "W") involved dissolution of $Zn(NO_3)_2\cdot6H_2O$ (35.7 g) and $Ga(NO_3)_3\cdot xH_2O$ (21.8 g) in deionized water (100 mL; solution D), NaOH (14.4 g) in deionized water (100 mL; 0.6 mol/L NaOH, solution E), and Na_2CO_3 (6.36 g) in deionized water (100 mL; 3.8 mol/L Na_2CO_3, solution F). Solutions D and E were added dropwise to solution F while maintaining the pH at 8. The mixture was stirred and aged for 20 h at 90 °C using an oil bath. The suspension was filtered, and the obtained solid was washed with deionized water and dried at 110 °C overnight to form the LDH precursor. This material was sieved into a fraction of 125–250 μm and then loaded into a quartz-tube reactor between two quartz-wool plugs. The material was exposed to pure NH_3 flow (200 mL/min) for nitridation and heated from room temperature to 800 °C (5 °C/min) for 1 h.

The solid-solution method (samples denoted by "S", used by the Domen group) is described in the literature and involves mixing stoichiometric amounts of ZnO (99.9%, Kanto Chemicals) and Ga_2O_3 (99.9%, High Purity Chemicals) under an NH_3 flow at 800 °C for 5–20 h [1,2,4]. In the present study, we used similar materials but from different suppliers, *i.e.*, ZnO (99.5%, AnalaR Normapur) and Ga_2O_3 (≥ 99.99%, Aldrich). The raw materials were mixed and placed in a quartz tube at a Zn:Ga molar ratio of *ca.* 1. The mixed powder was heated at 800 °C for 15 h in NH_3 (200 mL/min), resulting in a yellow powder. After nitridation for 15 h, the sample was cooled to room temperature in the NH_3 flow [4]. Typically, 1.08 g of Ga_2O_3 and 0.94 g of ZnO provided approximately 1 g of $(Ga_{1-x}Zn_x)(N_{1-x}O_x)$. $(Ga_{1-x}Zn_x)(N_{1-x}O_x)$ prepared as described in reference [23] was kindly provided by the Domen group [23] for Rh loading, Cr_2O_3 modification, and photocatalytic evaluation.

The resulting $(Ga_{1-x}Zn_x)(N_{1-x}O_x)$ materials are denoted by ZGON(x-y), where x is the synthetic method ("C", "W", or "S"), and y is the nitridation temperature (°C); for example, ZGON(W-800) is $(Ga_{1-x}Zn_x)(N_{1-x}O_x)$ synthesized by wet-precipitation and heated in NH_3 at 800 °C.

2.2. Synthesis of Rh NPs and photocatalysts

Uniformly sized PVP-stabilized Rh NPs were prepared according to the literature procedure [28]. A Rh precursor salt was reduced in the presence of PVP at different temperatures in an appropriate solvent. Small NPs were obtained by dissolving $RhCl_3 \cdot nH_2O$ (Aldrich; 10 mg) and PVP (M_n = 10 000, Sigma-Aldrich; 0.11 g) in water (2 mL) and 1,4-butanediol (Sigma-Aldrich; 3 mL). The mixture was then added to 1,4-butanediol (17 mL), which was preheated to 120 or 160 °C. To obtain larger NPs, $Rh(acac)_3$ (acac = acetylacetonate; Aldrich; 20 mg) and PVP (0.11 g) were dissolved in tetrahydrofuran (THF; Sigma-Aldrich; 2 mL) and 1,4-butanediol (3 mL), which was preheated to 160 or 220 °C. Each mixture was refluxed under a N_2 flow for 6 h and cooled to room temperature. A modified method was used to obtain very small (<3.5 nm) Rh particles. A solution consisting of $RhCl_3 \cdot nH_2O$ (10 mg), PVP (0.11 g), water (2 mL), and 1,4-butanediol (3 mL) was added to a suspension of ZGON (0.25 g) in preheated 1,4-butanediol (17 mL). The mixture was heated to 120 °C, refluxed under a N_2 flow for 6 h, and then cooled to room temperature. The loading of the support materials was carried out by dropwise addition of the Rh NP suspension to a suspension of ZGON (0.25 g) in glycerol (≥99%, Aldrich; 10 mL). The slurry was filtered, and the resulting powder was dried at 110 °C overnight. The catalysts are denoted by Rh(PVP)/ZGON(x-y)-z, where z is the average Rh NP size.

A portion of the catalyst was exposed to ultraviolet–ozone (UVO) to remove the organic capping agent. It was recently reported that such treatment removes PVP from the Rh NPs [29]. For this purpose, the sample (0.5 g) was dispersed on Al foil in a UVO chamber (PR 100, Ultra Violet Products. Inc.) and exposed to UV light and ozonated air at room temperature for 20 h [27]. The catalysts are denoted by Rh(PVP-UVO)/ZGON(x-y)-z.

A Cr_2O_3 shell was deposited on the Rh NPs [23,24,30]. Typically, Rh(PVP-UVO)/ZGON (0.15 g) was dispersed in an aqueous 0.2 mmol/L K_2CrO_4 solution (80 mL) in a double-walled glass vessel (held at 10 °C) with a quartz window on top. The reaction vessel was connected to a closed glass system to collect the produced H_2. Prior to photodeposition, the air in the vessel was completely removed by evacuation using a turbo drag pump. After evacuation, the solution was irradiated with visible light (λ = 420–630 nm) to reduce CrO_4^{2-} to Cr_2O_3. The irradiation was performed for 8 h. The final product was washed with deionized water and dried overnight at 110 °C. These samples are denoted by Cr-Rh(PVP-UVO)/ZGON(x-y)-z, where Cr indicates Cr_2O_3 addition.

For comparison, reference samples were prepared using $RhCl_3 \cdot nH_2O$ and K_2CrO_4 as precursors according to the photodeposition method used by the Domen group and others [31–33]. Typically, ZGON (0.25 g) was added to an aqueous solution (36 mL) containing $RhCl_3 \cdot nH_2O$ (13 mg) under stirring. Methanol (4 mL) was then added as a sacrificial reagent. The mixture was transferred to a glass vessel, and the air in the vessel was removed. After evacuation for 1.5 h, the suspension was irradiated with visible light (420–630 nm) for 4 h. The

evolution of H_2 with time was followed. The material was isolated from the solution by filtration. After drying overnight at 110 °C, it was dispersed in a K_2CrO_4 solution (0.2 mmol/L, 80 mL) for Cr_2O_3 photodeposition, following the same procedure as used for Cr-Rh(PVP-UVO)/ZGON. These catalysts are denoted by Cr-Rh/ZGON(S). The same Cr_2O_3 and Rh loading procedures were applied to the $(Ga_{1-x}Zn_x)(N_{1-x}O_x)$ sample provided by the Domen group; the resulting catalysts are denoted by Cr-Rh/ZGON(D).

2.3. Catalyst characterization

The metal was determined by inductively coupled plasma atomic emission spectroscopy (ICP-AES) using a Goffin Meyvis SpectroCirus CCD apparatus. The sample was dissolved under stirring and heating in a melt of $K_2S_2O_7$ in H_2SO_4 until a clear solution was obtained. The surface area of the support material was determined using a Micromeritics TriStar 3000 apparatus by N_2 physisorption at liquid N_2 temperature after outgassing the sample at 150 °C for 3 h. UV-Vis absorption spectra were obtained using a Shimadzu UV-2401 PC spectrometer in diffusion-reflectance mode with $BaSO_4$ as a reference. X-Ray diffraction (XRD) patterns were recorded using a D4 Endeavor diffractometer (Bruker) at a scan speed of 0.36°/min to determine the support structure. The morphologies of the support materials were studied by scanning electron microscopy (SEM) using an FEI Quanta 3D FEG instrument in high-vacuum mode at a low voltage (typically 10 mPa and 10 kV). Energy-dispersive X-ray spectroscopy (EDX) was performed using an EDAX instrument (AMETEK) with Genesis 700 software. Transmission electron microscopy (TEM) was performed using an FEI Tecnai 20 transmission electron microscope. Typically, a ground sample was suspended in pure ethanol, sonicated, and dispersed over a conventional carbon-coated Cu grid. The average particle size and particle size distribution were determined by measuring at least 150 metal particles.

X-ray photoelectron spectroscopy (XPS) was performed using a Thermo Scientific spectrometer, with an Al K_α monochromatic source. The spectra were recorded at an emission background pressure of 1×10^{-3} mPa. All the binding energies were referenced to the C 1s peak at 284.5 eV, related to surface adventitious carbon. Analysis and quantification of the measurements were performed using Casa-XPS software and Wagner's sensitivity factors.

X-ray absorption spectroscopy (XAS) was performed at the Dutch-Belgian beamline (Dubble) at the European Synchrotron Radiation Facility, Grenoble, France (storage ring 6.0 GeV, ring current 200 mA). Data were collected at the Rh K-edge in fluorescence mode with a solid-state detector. Energy selection was performed using a double crystal Si(111) monochromator. Background removal was carried out using standard procedures. EXAFS analysis was then performed with EXCURVE931 on k^3-weighted unfiltered raw data using the curved wave theory. Phase shifts were derived from *ab initio* calculations using Hedin-Lundqvist exchange potentials and Von Barth ground states. Energy calibration was carried out with Rh foil. The amplitude reduction factor, S_0^2, associated with central atom

shake-up and shake-off effects was set at 1.0 by calibration of the first- and second-shell Rh–Rh coordination numbers to 12 and 6, respectively, for the k^3-weighted EXAFS fitting of the Rh foil [25]. The structure of the Rh metal foil and the first two shells of the Fourier-transform (FT) EXAFS spectrum of Rh_2O_3 corresponded well to the literature data [34]. The near-edge regions of the absorption spectra of these reference compounds were used to fit the near-edge regions of the catalysts. Spectra at the Rh K-edge were recorded in a stainless-steel controlled-atmosphere cell. Typically, the sample (80 mg) was pressed in a holder and placed in the cell. Carbon foils were held between two high-purity carbon spacers. High-purity gases (He and O_2) were delivered by thermal mass flow controllers. The total gas flow was kept at 50 mL/min [26]. After recording two EXAFS spectra of the sample at room temperature under a He flow, the sample was heated in a 3% O_2/He flow to a final temperature of 300 °C, while recording the XANES spectra.

2.4. Catalytic activity measurements

2.4.1. Photocatalytic H_2 production

Photocatalytic H_2 production by water splitting was performed using the setup described in detail elsewhere [27]. Typically, the catalyst (0.1 g) was added to a closed reactor vessel containing deionized water (36 mL) and methanol (4 mL; sacrificial electron donor) under stirring. After complete removal of the air from the vessel by evacuation for 30 min, a light source (Xe Arc Lamp, Oriel) was switched on, and the suspension was irradiated with visible light (420–630 nm, 320 mW/cm²) for at least 4 h. Tests were repeated at least three times. The setup performance was regularly checked using a 0.3 wt% Pt/TiO$_2$ reference photocatalyst. H_2 gas evolved from water splitting was analyzed using an online gas chromatograph (GC; ATI UNICAM GC-610, Shincarbon, thermal conductivity detector).

2.4.2. Oxidation reactions

The catalytic activities in the oxidation of CO and H_2 with molecular O_2 were determined in a parallel ten-flow microreactor system equipped with thermal mass flow controllers and an online GC (Interscience, Porapak Q, Molecular sieve 5A, thermal conductivity detector). Typically, the SiC-diluted catalysts were loaded into quartz reactor tubes [25]. Prior to the activity measurements, the samples were dried in a He flow (10 °C/min) from room temperature to 110 °C for 1 h. The reactor was cooled in He to the reaction temperature. At each reaction temperature, rates were determined for 1.5 h, during which no deactivation was observed. For CO (H_2) oxidation, the feed contained 2 vol% CO (H_2) and O_2 with O_2/CO = 1 (O_2/H_2 = 1), balanced by He, at gas hourly space velocities between 7×10^4 and 1×10^5 h^{-1} in the temperature range 40–210 °C (30–230 °C). The activation energy was determined on the basis of measurements in which the conversion was below 20%.

3. Results and discussion

3.1. Catalyst synthesis and characterization

3.1.1. Support materials

The basic characterization results for the precursor and ZGON(C) samples are shown in Fig. 1. XRD shows that the precursor mainly consists of crystalline $ZnGa_2O_4$ spinel. It is con-
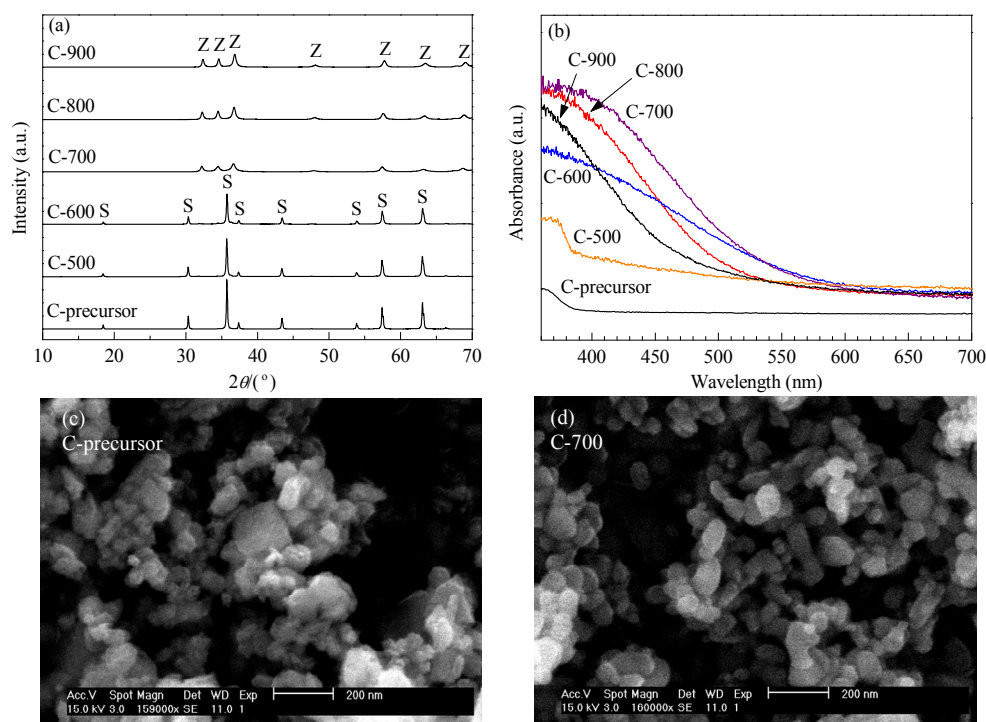

Fig. 1. XRD patterns (a) (Z = ZGON, S = spinel), UV-Vis spectra (b), and SEM images (c, d) of spinel precursor and ZGON(C) at different nitridation temperatures.

verted to the ZGON phase by nitridation. Nitridation takes place above 600 °C, and the XRD patterns of the spinel precursor and the ZGON materials agree with the literature data [13,19]. The UV-Vis spectra show increased visible-light absorption by the nitrided samples. When the ZGON phase has been fully formed, the absorption edge decreases with increasing nitridation temperature. Treatment at 700 °C shows the highest visible-light response with an absorption edge at *ca.* 600 nm. These results are consistent with those reported by Ward et al. [18]. The SEM images show that the particle size of the spinel precursor is in the range 100–200 nm. The size and shape did not change after nitridation at 700 °C.

The synthetic conditions and sample compositions are listed in Table 1. The starting solid solution and the ZnGa2O4 spinel both have a Zn/Ga ratio of 2.7. No Zn was lost during spinel formation by this method. The Zn/Ga ratio decreases with increasing nitridation temperature as a result of Zn loss by evaporation. The N content of the spinel precursor is very low and remains almost constant following nitridation at 500 and 600 °C. At higher temperatures, it increases substantially up to almost 29 at% at 900 °C. The surface areas of the ZnGa-LDHs, ZnGa2O4 spinel precursors, and nitrided ZGON materials are 42, 13, and 12–14 m²/g, respectively. The surface area therefore decreases during thermal conversion of the LDH precursor to the ZnGa2O4 spinel, but nitridation has little effect. This is consistent with the SEM results.

Figure 2 shows the basic characterization results for the ZGON(S-800) and ZGON(W-800) samples. The XRD patterns of these samples are very similar to that recorded for ZGON(C-800). The UV-Vis absorption edge at 470 nm for ZGON(S-800) is lower than that, located at *ca.* 590 nm, for ZGON(W-800). ZGON(C-800) has an absorption edge at *ca.* 520

Table 1
Synthesis details, surface areas, and EDX results for ZGON support materials.

Synthesis method	Nitridation		Surface area (m²/g)	Surface atomic ratio[a]		N surface content (at%)
	T/°C	*t*/h		Zn/Ga	N/Ga	
C	ZnGa-LDH	—	42	—	—	—
	ZnGa2O4 spinel		13	2.7	0.23	6.2
	500	10	14	0.93	0.14	5.8
	600	10	12	0.30	0.32	6.8
	700	10	—	0.09	0.43	15.6
	800	10	13	0.06	0.55	24.4
	900	10	12	0.02	0.55	28.5
W	LDH precursor	—	83	2.1	0.58	13.2
	800	1	19	2.0	1.00	12.5
S	800	15	10	0.13	0.79	37.9

[a] Determined by EDX.

nm. The SEM images show that ZGON(S) consists of long rods with irregular surfaces, whereas ZGON(W-800) mainly contains hexagonal nanoplates of similar morphology to those described by Wang et al. [21]. The surface area of ZGON(S) is 10 m²/g, similar to that of ZGON(C-800). ZGON(W-800) has a slightly higher surface area (19 m²/g), which originates from the higher surface area of the LDH precursor (83 m²/g). The Zn/Ga and N/Ga ratios of 0.13 and 0.79, respectively, for ZGON(S) are consistent with the values reported by Maeda et al. [1,2]. These ratios are slightly higher than that for ZGON(C-800). Both are substantially lower than the Zn/Ga ratio of 2.0 for ZGON(W-800). The reasons for the high Zn content of the latter sample are the short nitridation time and the different synthetic procedure, which does not include calcination and washing steps.
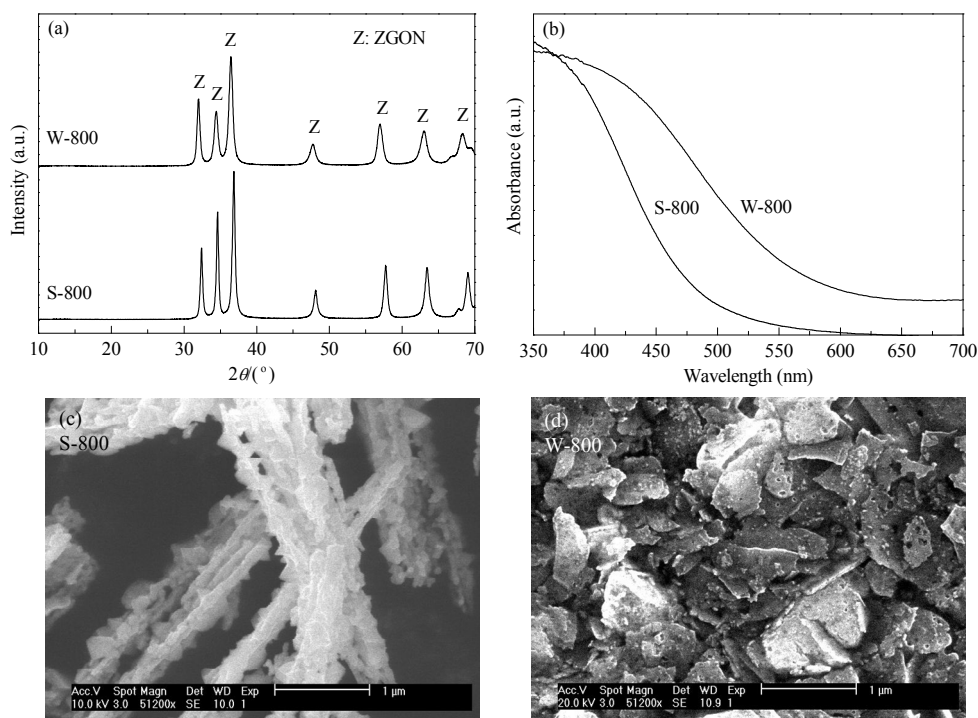

Fig. 2. XRD patterns (a), UV-Vis spectra (b), and SEM images (c, d) of ZGON(S-800) and ZGON(W-800).

3.1.2. PVP-stabilized Rh NPs

The synthetic conditions for the PVP-stabilized Rh NPs are listed in Table 2. The average particle size and distribution of the unsupported systems are similar to those reported earlier [27,35]. ZGON(W-800) was used to support these Rh(PVP) NPs because of its favorable absorption edge and relatively high surface area. No noticeable changes in the Rh NP shapes and sizes were observed by TEM for the supported systems (Fig. 3).

3.1.3. UVO treatment and Cr₂O₃ photodeposition

Instead of calcination, which may negatively affect the size distribution and the semiconductor N content, UVO treatment was performed on a portion of each catalyst to remove PVP from the Rh NPs [36]. After this treatment, the Rh NPs were coated with Cr_2O_3 by photodeposition. Typically, such low-temperature treatments do not affect the NP size [29]. The EXAFS data shown below indicate that the Rh NPs do not sinter although some further oxidation takes place, depending on their initial size. Elemental analysis shows that the samples do not contain much Cr after photodeposition (Table 2). Maeda et al. [33,37] reported a Cr content of 0.75 wt% for a catalyst containing 0.31 wt% Rh. The finding that no Cr_2O_3 was deposited may be explained by the absence of photogeneration of the electron-hole pairs required for the reduction of chromate on the Rh NPs. The Ga and Zn oxidation states of several samples, including that provided by the Domen group, were determined

Table 3

Surface compositions of ZGON-based catalysts derived from XPS Ga $2p_{3/2}$, Zn $2p_{3/2}$, O $1s$, N $1s$, and Rh $3d$ peak areas.

Catalyst	Surface atomic ratio			Rh (at%)	N (at%)
	Zn/Ga	O/Ga	N/Ga		
ZGON(D)	0.10	1.6	2.6	—	49.0
ZGON(S)	0.07	2.8	2.8	—	41.5
ZGON(W-800)	2.0	4.9	2.5	—	24.0
Rh(PVP-UVO)/ZGON(W-800)-2.3	1.8	6.1	2.5	1.1	21.8
Rh(PVP-UVO)/ZGON(W-800)-7.5	1.5	4.0	2.4	0.4	26.6
Cr-Rh(PVP-UVO)/ZGON(W-800)-7.5	1.5	5.0	2.5	0.5	24.7

using XPS (data not shown). The main features of Ga $2p_{3/2}$ and Zn $2p_{3/2}$ are at 1118.8 and 1022.2 eV, respectively, in agreement with the results reported by Maeda et al. [2,33,38]. The binding energies of Ga $2p_{3/2}$ and Zn $2p_{3/2}$ of the reference GaN and ZnO materials are 1118.8 and 1022.7 eV, respectively [2]. The oxidation states of Ga and Zn in the mixed oxides are therefore similar to those of Ga^{3+} and Zn^{2+} in GaN and ZnO, respectively. The XPS results confirm that no Cr is present in the Cr-Rh(PVP-UVO)/ZGON(W-800) sample after photodeposition (not shown). The surface atomic ratios of the support elements derived from XPS analysis are listed in Table 3. The corresponding Zn/Ga ratios and N contents for ZGON(S) and ZGON(W-800) are in reasonable agreement with the EDX data (Table 1). The Zn/Ga ratio of ZGON(D) matches that reported by Maeda et al. [2]. Overall, the surface results for ZGON(S) are

Table 2

Details of Rh NP synthesis and properties of ZGON(W-800)-supported Rh catalysts.

Catalyst	Rh NPs synthesis conditions			ZGON-supported catalysts		
	Precursor	Solvent	$T_{reduction}$ (°C)	Rh [a] (wt%)	Cr [a] (wt%)	d_{Rh} [b] (nm)
Rh(PVP)/ZGON(W-800)-2.3 [c]	RhCl₃·nH₂O	H₂O	120	1.25	—	2.3 ± 0.5
Rh(PVP)/ZGON(W-800)-3.7	RhCl₃·nH₂O	H₂O	120	1.28	—	3.7 ± 0.6
Rh(PVP)/ZGON(W-800)-5.4	RhCl₃·nH₂O	H₂O	160	1.16	—	5.4 ± 2.0
Rh(PVP)/ZGON(W-800)-7.5	Rh(acac)₃	THF	160	0.64	—	7.5 ± 1.2
Rh(PVP)/ZGON(W-800)-9.3	Rh(acac)₃	THF	220	1.78	—	9.3 ± 2.0
Cr-Rh(PVP-UVO)/ZGON(W-800)-7.5	—	—	—	0.64	0.03	—

[a] Determined by ICP-AES. [b] Estimated average Rh NP size from TEM. [c] RhCl₃ solution was reduced in the presence of ZGON.
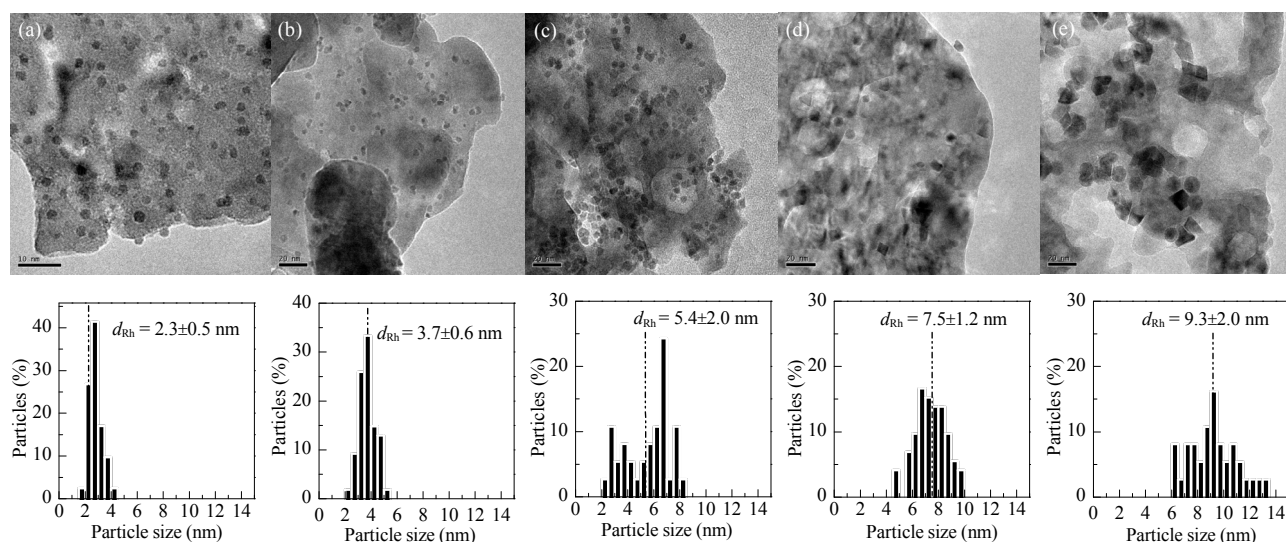

Fig. 3. Representative TEM images and particle size distributions of Rh(PVP)/ZGON(W-800) with 2.3 (a), 3.7 (b), 5.4 (c), 7.5 (d), and 9.3 nm (e) Rh NPs.
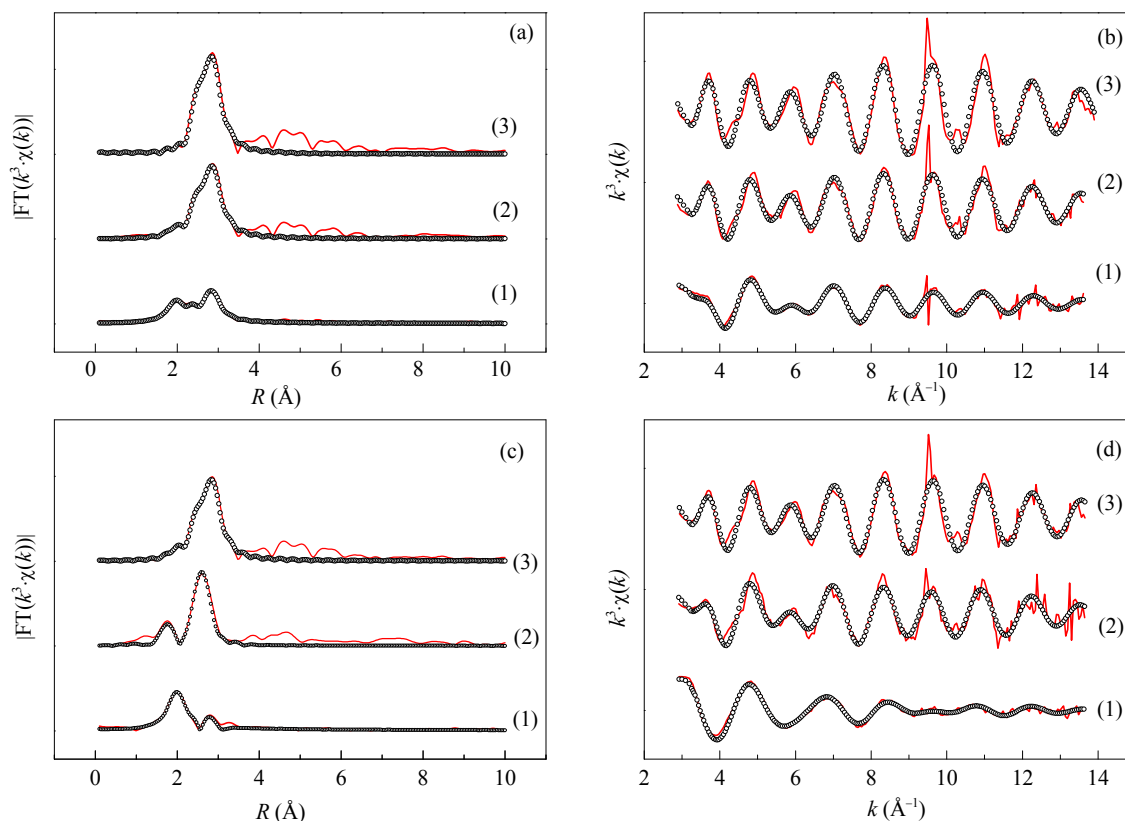
Fig. 4. Experimental (solid line) and fitted (open points) (a, c) FT EXAFS functions and (b, d) k^3-weighted EXAFS oscillations of fresh (in pure He at room temperature) Rh(PVP)/ZGON(W-800) (a, b) and Rh(PVP-UVO)/ZGON(W-800) (c, d) with 2.3 (1), 5.4 (2), and 9.3 nm (3) Rh NPs.

similar to those for ZGON(D), whereas those for ZGON(W) are very different, with the exception of the N/Ga ratio.

Figure 4 shows the experimental and fitted FT EXAFS spectra and k^3-weighted $\chi(k)$ EXFAS functions of Rh/ZGON(W-800) samples with 2.3, 5.4, and 9.3 nm Rh NPs. The fitted parameters are summarized in Table 4. In He at room temperature, the FT EXAFS spectra contain a first Rh–Rh shell at a coordination distance (R) of 2.69 Å, which is close to that in bulk Rh in a reference Rh foil [25]. The coordination number (N) of this shell increases with increasing average Rh particle size. The spectra of fresh Rh(PVP)/ZGON(W-800)-2.3 and Rh(PVP)/ZGON(W-800)-5.4 show Rh–O shells at distances of *ca.* 2 Å. This contribution is more distinct in the spectra of the UVO-treated samples, especially for smaller Rh particles. The quantitative parameters listed in Table 4 support these observations. Overall, smaller particles are more prone to oxidation than larger ones, consistent with literature reports [25,26]. It can also be also seen that the Rh–Rh coordination shell typically decreases, indicating that oxidation only took place during the UVO treatment, without extensive sintering of the particles.

Figure 5 shows the near-edge spectra of the Rh(PVP-UVO)/ZGON(W-800) set during oxidation at 140 °C. The white-line feature of the Rh catalysts increases with decreasing Rh NP size. The near-edge region of the catalyst containing small Rh NPs is similar to that of the reference Rh_2O_3, whereas the near-edge region of the large Rh NPs resembles that of the foil [25,26]. Table 5 lists the fractions of oxidic Rh (f_{Rh3+}) before and

during oxidation with increasing temperature. The fraction of oxidic Rh increases with decreasing Rh NP size and UVO treatment of the fresh samples, which is consistent with the EXAFS results. However, at higher oxidation temperatures, the fraction no longer increases. This seems to be related to the support properties [25]. The Rh oxidation degree of the sample pre-

Table 4

Fitted parameters of k^3-weighted EXAFS spectra at Rh K-edge of fresh ZGON-based catalysts.

Catalyst	EXAFS analysis *			
	Shell	R (Å)	N	$\Delta\sigma^2$ (Å^2)	E_0 (eV)
Rh(PVP)/ZGON(W-800)-2.3	Rh–O	2.019	2.33	0.007	
	Rh–Rh	2.684	3.81	0.007	0.7
Rh(PVP)/ZGON(W-800)-5.4	Rh–O	1.992	0.88	0.005	
	Rh–Rh	2.690	7.16	0.005	–0.3
Rh(PVP)/ZGON(W-800)-9.3	Rh–Rh	2.690	8.78	0.005	0.1
Rh(PVP-UVO)/ZGON(W-800)-2.3	Rh–O	2.043	4.14	0.006	
	Rh–Rh	2.697	0.92	0.005	0.2
Rh(PVP-UVO)/ZGON(W-800)-3.7	Rh–O	2.041	2.89	0.006	
	Rh–Rh	2.695	3.19	0.005	–0.6
Rh(PVP-UVO)/ZGON(W-800)-5.4	Rh–O	2.013	1.89	0.002	
	Rh–Rh	2.697	5.69	0.005	–0.6
Rh(PVP-UVO)/ZGON(W-800)-7.5	Rh–O	2.002	1.18	0.005	
	Rh–Rh	2.690	6.37	0.004	–0.1
Rh(PVP-UVO)/ZGON(W-800)-9.3	Rh–O	2.014	1.09	0.007	
	Rh–Rh	2.687	7.36	0.005	–0.2

* Only the first Rh–O and Rh–Rh shells were fitted; Δk = 2.5-12 Å^{-1}; estimated error in R ± 0.01 Å, N ± 20%, $\Delta\sigma^2$ ± 10%; the R-factor was below 30%.
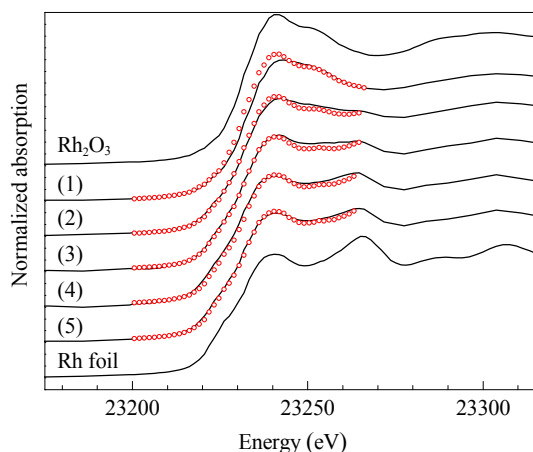
Fig. 5. Rh K-edge XANES spectra recorded during oxidation at 140 °C of Rh(PVP-UVO)/ZGON(W-800) with 2.3 (1), 3.7 (2), 5.4 (3), 7.5 (4), and 9.3 nm (5) Rh NPs. Rh_2O_3 and Rh foil references are included for comparison. The dots represent the results of XANES fitting by linear combinations of the two references.

pared by Rh photodeposition is slightly larger than those of the Rh particles prepared using the PVP method.

3.2. Catalyst activity measurements

3.2.1. Photocatalytic H_2 production

Photocatalytic H_2 production by water splitting was performed using the (Cr-)Rh(PVP-UVO)/ZGON(W-800) materials and reference materials. The setup was regularly tested using a reference catalyst (25 mg of TiO_2 (P25) containing 0.3 wt% Pt loaded by photodeposition), which gave H_2 production rates of around 2100 μmol h^{-1} g$_{cat}$$^{-1}$, in good agreement with other studies [39,40]. The sample provided by the Domen group, to which 1 wt% Rh was added by photodeposition, gave a H_2 production rate of only 0.3 μmol h^{-1} g$_{cat}$$^{-1}$, which is in line with the results reported by Maeda et al. [23]. After photodeposition using a K_2CrO_4 solution, the Cr-Rh/ZGON(D) activity increased to 3.7 μmol h^{-1} g$_{cat}$$^{-1}$. This confirms that Cr_2O_3 deposition improves the water-splitting efficiency of the Rh/ZGON sample. However, the activity is almost two orders of magnitude lower than the values reported by Maeda et al. [23]. The reason for

Table 5

Rh K-edge XANES spectra fitting results; fractions of oxidic Rh (f_{Rh3+}) in ZGON-supported Rh catalysts in fresh state and during oxidation from room temperature to 300 °C.

Catalyst	f_{Rh3+}* (%)						
	He	T (°C) in O_2/He					
	RT	RT	60	110	140	200	300
Rh(PVP)/ZGON(W-800)-2.3	44	—	—	—	—	—	—
Rh(PVP)/ZGON(W-800)-5.4	19	—	—	—	—	—	—
Rh(PVP)/ZGON(W-800)-9.3	10	—	—	—	—	—	—
Rh(PVP-UVO)/ZGON(W-800)-2.3	89	92	92	92	93	93	95
Rh(PVP-UVO)/ZGON(W-800)-3.7	60	60	63	64	64	64	64
Rh(PVP-UVO)/ZGON(W-800)-5.4	39	40	40	41	41	42	42
Rh(PVP-UVO)/ZGON(W-800)-7.5	27	27	27	27	28	28	28
Rh(PVP-UVO)/ZGON(W-800)-9.3	24	23	23	23	23	25	25

*Estimated error in f ± 5%.

this is unclear. Our ZGON(S)- and ZGON(W)-based catalysts, namely Cr-Rh/ZGON(S), Cr-Rh/ZGON(W), and Cr-Rh(PVP-UVO)/ZGON(W), did not show any photocatalytic activity, and these results were reproducible. The absence of Cr_2O_3 deposition, verified by ICP analysis, is consistent with the absence of photocatalytic activities of the parent ZGON materials. The reason for the absence of photocatalytic activity is unclear. Our synthetic methods were the same as those used by the Domen group [41]. ZGON(S) was prepared in the same way, but the Zn and surface N contents are slightly different. ZGON(W) contains much more Zn than the sample prepared using the solid-state method. Although we cannot draw firm conclusions at present, we speculate that slight differences in the bulk and surface compositions explain the absence of activity for our samples. There have been a large number of literature reports on the use of ZGON-type materials, but only those reported by the Domen group (cited earlier), Hahn et al. [42], Busser et al. [43], and Chorkendorff's group in collaboration with the Domen group [44] reported good photocatalytic water-splitting activities. This highlights the tight control needed to prepare active ZGON semiconductor materials. In the next section, we explore the oxidation of H_2 as a model for reverse water splitting to produce H_2. We first evaluated the activities of these samples in CO oxidation, given recent reports on the size and oxidation-state dependences of supported Rh NPs [25].

3.2.2. CO oxidation

CO oxidation was carried out using the Rh(PVP-UVO)/ZGON(W-800) catalysts (Table 6). The reaction rate strongly decreases with increasing particle size. When corrected for dispersion, the turnover frequencies (TOFs) are much less dependent on the particle size, although the two catalysts with the largest average particle size are significantly less active than the ones containing smaller particles. The activity of Rh(PVP)/ZGON(W-800)-2.3 before UVO treatment is higher than that after UVO treatment. The particle size dependence for the present Rh/ZGON set is less prominent than the dependences observed for Rh/CeO$_2$ catalysts [25]. Song et al. [45] have shown that the rate of CO oxidation for a surface rhodium oxide film on CeO_2 is much higher than that of Rh metal NPs. The reaction involves the CeO_2 support, which oxidizes partly reduced rhodium oxide clusters. In the present study, the support is probably not involved in the catalytic CO oxidation reaction because ZnO does not reduce at relatively low reaction temperatures. Grass et al. [28] also concluded that the active phase for CO oxidation of unsupported Rh NPs is the surface rhodium

Table 6

CO oxidation activity and activation energies for selected set of ZGON-based catalysts (O$_2$/CO ratio = 1; T = 160 °C).

Catalyst	r (mol mol$_{Rh}$$^{-1}$ h^{-1})	TOF (h^{-1})	E_{app} (kJ/mol)
Rh(PVP)/ZGON(W-800)-2.3	292	611	93
Rh(PVP-UVO)/ZGON(W-800)-2.3	151	315	90
Rh(PVP-UVO)/ZGON(W-800)-3.7	85	287	77
Rh(PVP-UVO)/ZGON(W-800)-5.4	67	329	81
Rh(PVP-UVO)/ZGON(W-800)-7.5	32	217	80
Rh(PVP-UVO)/ZGON(W-800)-9.3	26	218	82

oxide. Smaller particles are more prone to form a surface oxide under the reaction conditions used than larger particles are. Assuming that the ZGON support is not involved in the CO oxidation reaction, the decreasing TOF with increasing Rh particle size for the Rh/ZGON set is in line with these results [25,28]. This is also consistent with the higher oxidation degree of smaller particles, shown by XAS. The activation energy for CO oxidation decreases with increasing particle size. The activities of the present catalysts are lower than those for dried Rh(PVP)/SBA-15 catalysts [46]. Consistent with our analysis, little influence of the particle size on the activation energy has been observed [46,47]. The activity of the Rh(PVP-UVO)/ZGON(W-800)-2.3 sample is about two times lower than that before the UVO treatment. This is in contrast to the activity enhancement achieved by UVO treatment of Pt NP systems stabilized with various organic molecules [48]. The difference is probably that Pt oxidation is less important than Rh oxidation, so capping agents decrease the performance of Pt more than that of Rh.

3.2.3. H_2 oxidation

We then investigated the catalytic activities of these Rh NP samples in the oxidation of H_2 (Fig. 6). The Rh(PVP–UVO) samples with smaller Rh particles have lower reaction rates than catalysts containing larger Rh particles. At low temperature, the Rh(PVP) catalysts display higher catalytic activities than the Rh(PVP-UVO) ones, but the differences become smaller with increasing temperature. For instance, the activities of the catalysts of average particle size 2.3 nm before and after UVO treatment are similar at temperatures higher than 165 °C. The lower activities of the UVO-treated samples are probably the result of more extensive oxidation of the NPs (Table 5). All catalysts with an average Rh size smaller than ca. 7 nm attained similar high reaction rates at temperatures above 165 °C. For Rh NPs larger than 7 nm, the rate increased with increasing particle size. It is therefore concluded that the preferred active phase of these catalysts in H_2 oxidation is the metallic phase.
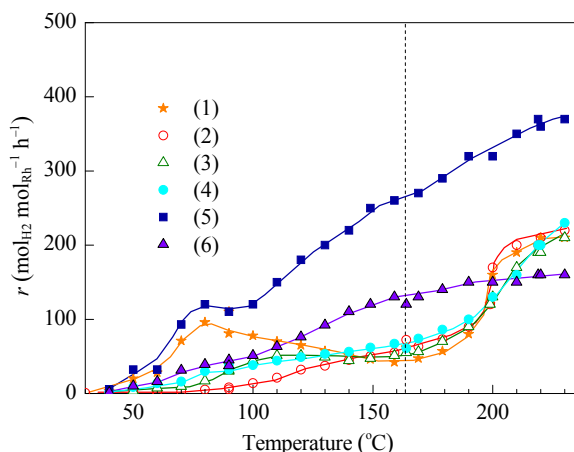

Fig. 6. H_2 oxidation (O_2/H_2 = 1) rates as a function of reaction temperature over dried Rh(PVP)/ZGON(W-800) (1) and Rh(PVP-UVO)/ZGON (W-800) with 2.3 (2), 3.7 (3), 5.4 (4), 7.5 (5), and 9.3 nm (6) Rh NPs. The data point at 165 °C (dashed line) was determined after reaction at 230 °C (T_{max}).

This explains the higher activities of the larger Rh NPs. The strong increase in the activities of small particles during oxidation above 165 °C results from the reduction of the rhodium oxide phase. It is reasonable to assume that metal NPs would also be active sites in H_2 generation during photocatalytic water splitting. Shimura et al. [49,50] have investigated the effects of the oxidation states of Rh NPs supported on $Sr_2Ti_6O_{13}$ in the photocatalytic water-splitting reaction, and found that Rh metal catalyzes photocatalytic H_2 production better than rhodium oxide does. Our earlier research on Rh particles supported on g-C_3N_4 also demonstrated that Rh metal particles are preferable for the H_2 production reaction [27]. To summarize, for H_2 oxidation and its reverse reaction, the Rh metal phase is more active than the rhodium oxide phase in NPs.

3.3. General discussion

We synthesized ZGON(W) catalysts with higher surface areas and Zn/Ga ratios than those reported by the Domen group. Despite their favorable light-absorbing properties shown by UV-Vis spectroscopy, ZGON(W-800) and ZGON(S) loaded with Rh NPs via the PVP method and photodeposition of Rh, respectively, are not active in photocatalytic H_2 production under visible-light irradiation. The most likely reason is the differences in the bulk and surface compositions of the final ZGON materials. For ZGON(W-800), we obtained a similar crystalline structure (Fig. 2(a)), UV-Vis absorption spectrum (Fig. 2(b)), Zn/Ga ratio, and N surface content (Table 1) as Wang et al. [21] who did not report photocatalytic activity measurements for their samples. For ZGON(S), we found that the structure, surface area, and Zn/Ga and N/Ga ratios are close to those of the materials reported by the Domen group. A notable difference in the XPS spectra (not shown) was a slight shift of the Ga and Zn $2p_{3/2}$ peaks of the sample provided by the Domen group, ZGON(D), to lower binding energies compared with ZGON(S). This is consistent with slightly different bulk and surface compositions. Although ZGON(S) did not show any photocatalytic activity, the Domen's sample produced a small amount of H_2 after loading with Rh, and H_2 production was further enhanced after Cr_2O_3 photodeposition. Nonetheless, its activity is much lower than that reported by the Domen group. From the absence of Cr_2O_3 deposition on Rh/ZGON(W-800) and the other ZGON(S)-based samples, we infer that the photogenerated electron–holes are not able to reduce the chromate. This is consistent with the absence of photocatalytic H_2 production before Cr_2O_3 deposition, and points to a problem with electron transfer from the ZGON light absorber to the cocatalyst. In our study, we used PVP-stabilized Rh NPs. Although the use of PVP might cause the absence of electron transfer from the support to the cocatalyst, we found that conventional photodeposition of Rh on the semiconductor did not produce active photocatalysts either. In the studies by groups other than the Domen group that achieved photocatalytic H_2 production by water splitting using these materials, the synthetic procedures and/or photocatalytic performance were different from those reported by the Domen group. For instance, Maeda et al. [1,2] used pure NH_3 and Busser et al. [43] used 10% NH_3/He for nitridation,

and their products are also photoactive. Hahn et al. [42] used the same procedures as Maeda et al. [1,2] and obtained a photocatalytic H_2 production of *ca.* 13 μmol h^{-1} g$_{cat}^{-1}$, which is only slightly higher than the activity of our Cr-Rh/ZGON(D) (3.7 μmol h^{-1} g$_{cat}^{-1}$). The activity reported by Hahn et al. [42] is also two orders of magnitude lower than the activity reported by the Domen group [23]. Maeda et al. [41] suggested that the pressure during nitridation and structures of the starting materials can influence the photocatalytic performance of the ZGON product. We therefore speculate that tight control of ZGON synthesis is crucial to obtain photoactive materials that can be used for photocatalytic water splitting. From the above analysis, we infer that it is probable that small differences in the surface composition sometimes inhibit the photocatalytic performance. In addition to the exact ZGON composition, the contact with the Rh NPs may also affect the final performance.

The CO oxidation results demonstrate that smaller Rh particles are more easily oxidized than larger ones. The catalytic activity increases with increasing oxidation degree of the Rh phase, in accordance with previous results [25,28]. This confirms that the rhodium oxide phase is more active for CO oxidation than Rh NPs are [25,28,46]. The difference compared with the study by Ligthart et al. [25] is that ZGON is not reducible. This results in a less pronounced dependence of the reaction rate on the Rh particle size. For H_2 oxidation, we observe the opposite trend. Rh metal particles are more active than oxidic ones. Small particles, which are oxidic, therefore show low reaction rates, and larger ones with at most a thin oxide layer, which can be easily removed, have high H_2 reaction rates. This is consistent with the common notion that metal NPs catalyze H_2 combustion best. Nilekar et al. [51] suggested that removal of adsorbed O from the surface was a significant step in the reaction mechanism: O* + H* → OH* + * or O_2H* + * → O* + OH*, followed by OH* + H* → H_2O + 2*. Among these elementary reactions, hydrogenation of OH (OH*+ H* → H_2O + 2*) is expected to be facile. Also, dissociation of H_2 and O_2 on Rh metal surfaces should be easy. O* hydrogenation (O* + H* → OH* + *) is difficult on Rh metal. The Rh–O bond in rhodium oxide is stronger than the Rh–O bond of an O adatom on Rh metal, consistent with the higher activity of Rh metal NPs in H_2 combustion. Clearly, above *ca.* 165 °C, the activity of the smaller particles strongly increases because the particles become metallic, in line with the typical reduction temperatures of rhodium oxide, at around this temperature [26]. Although H_2 formation also occurs in photocatalytic water splitting, some differences should be noted. The photogenerated electrons reduce protons at the NP metal surfaces. Shimura et al. [49,50] and Maeda et al. [37] suggested that electron extraction from the conduction band of ZGON by rhodium oxide is less efficient than that achieved by Rh metal. This suggests that rhodium oxide cocatalyst reduction is necessary for obtaining active photocatalysts.

4. Conclusions

Mixed $(Ga_{1-x}Zn_x)(N_{1-x}O_x)$ materials were synthesized by co-precipitation, wet-precipitation, and solid-solution methods. The textural and light-absorption properties and chemical compositions of these materials were compared. PVP-stabilized Rh NPs with sizes in the 2–9 nm range were loaded onto wet-precipitated $(Ga_{1-x}Zn_x)(N_{1-x}O_x)$. Small Rh particles were more prone to oxidation than larger ones. UVO treatment was used to remove PVP and enhanced oxidation. All the samples were inactive for photocatalytic H_2 production. The lower activity than a reference sample provided by the Domen group is explained for some samples by subtle differences in the bulk and surface compositions, stressing the need for tight control of the synthesis of $(Ga_{1-x}Zn_x)(N_{1-x}O_x)$. Small, more oxidic Rh NPs are more active in CO oxidation than larger metal ones, whereas the reverse holds for the H_2 oxidation reaction. Under H_2 oxidation conditions, smaller particles become very active at elevated temperatures when the surface is reduced.

References

[1] Maeda K, Takata T, Hara M, Saito N, Inoue Y, Koboyashi H, Domen K. *J Am Chem Soc*, 2005, 127: 8286
[2] Maeda K, Teramura K, Takata T, Hara M, Saito N, Toda K, Inoue Y, Kobayashi H, Domen K. *J Phys Chem B*, 2005, 109: 20504
[3] Maeda K, Teramura K, Lu D L, Takata T, Saito N, Inoue Y, Domen K. *Nature*, 2006, 440: 295
[4] Yashima M, Maeda K, Teramura K, Takata T, Domen K. *Chem Phys Lett*, 2005, 416: 225
[5] Yashima M, Maeda K, Teramura K, Takata T, Domen K. *Mater Trans*, 2006, 47: 295
[6] Sun X J, Maeda K, Le Faucheur M, Teramura K, Domen K. *Appl Catal A*, 2007, 327: 114
[7] Hirai T, Maeda K, Yoshida M, Kubota J, Ikeda S, Matsumura M, Domen K. *J Phys Chem C*, 2007, 111: 18853
[8] Maeda K, Teramura K, Domen K. *J Catal*, 2008, 254: 198
[9] Hisatomi T, Maeda K, Lu D L, Domen K. *ChemSusChem*, 2009, 2: 336
[10] Hisatomi T, Miyazaki K, Takanabe K, Maeda K, Kubota J, Sakata Y, Domen K. *Chem Phys Lett*, 2010, 486: 144
[11] Meada K, Hashiguchi H, Masuda H, Abe R, Domen K. *J Phys Chem C*, 2008, 112: 3447
[12] Boppana V B R, Doren D J, Lobo R F. *J Mater Chem*, 2010, 20: 9787
[13] Zou L, Xiang X, Wei M, Li F, Evans D G. *Inorg Chem*, 2008, 47: 1361
[14] Moriya Y, Takata T, Domen K. *Coord Chem Rev*, 2013, 257: 1957
[15] Adeli B, Taghipour F. *ECS J Solid State Sci Technol*, 2013, 2: Q118
[16] Han W Q, Liu Z X, Yu H G. *Appl Phys Lett*, 2010, 96: 183112
[17] Lee K, Tienes B M, Wilker M B, Schnitzenbaumer K J, Dukovic G. *Nano Lett*, 2012, 12: 3268
[18] Ward M J, Han W Q, Sham T K. *J Phys Chem C*, 2013, 117: 20332
[19] Li X H, Shao C L, Wang D, Zhang X, Zhang P, Liu Y C. *Ceram Int*, 2014, 40: 3425
[20] Li F, Duan X. *Struct Bond*, 2006, 119: 193
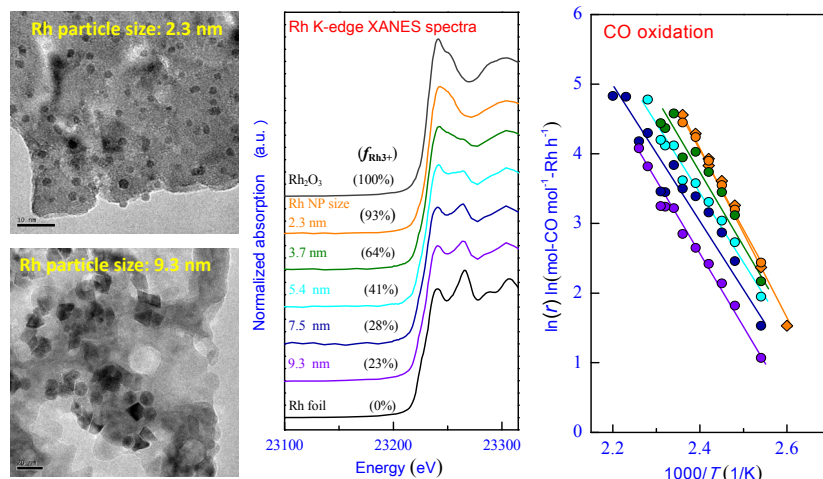[21] Wang J P, Huang B B, Wang Z Y, Wang P, Cheng H F, Zheng Z X, Qin

Graphical Abstract

Size dependence of photocatalytic oxidation reactions of Rh nanoparticles dispersed on $(Ga_{1-x}Zn_x)(N_{1-x}O_x)$ support

Yi Zhang, D. A. J. Michel Ligthart, Peng Liu, Lu Gao, Tiny M. W. G. M. Verhoeven, Emiel J. M. Hensen*
Eindhoven University of Technology, The Netherlands

The influence of Rh particle size on the (photo)catalytic performance of ZnO/GaN-supported Rh was investigated. Small oxidic particles were most active in CO oxidation, and large metal ones were most active in H_2 oxidation.

X Y, Zhang X Y, Dai Y, Whangbo M H. *J Mater Chem*, 2011, 21: 4562

[22] Mapa M, Thushara K S, Saha B, Chakraborty P, Janet C M, Viswanath R P, Nair C M, Murty K V G K, Gopinath C S. *Chem Mater*, 2009, 21: 2973

[23] Maeda K, Sakamoto N, Ikeda T, Ohtsuka H, Xiong A K, Lu D L, Kanehara M, Teranishi T, Domen K. *Chem Eur J*, 2010, 16: 7750

[24] Ikeda T, Xiong A K, Yoshinaga T, Maeda K, Domen K, Teranishi T. *J Phys Chem C*, 2013, 117: 2467

[25] Ligthart D A J M, van Santen R A, Hensen E J M. *Angew Chem Int Ed*, 2011, 50: 5306

[26] Ligthart D A J M, van Santen R A, Hensen E J M. *J Catal*, 2011, 280: 206

[27] Zhang Y, Ligthart D A J M, Quek X Y, Gao L, Hensen E J M. *Int J Hydrogen Energy*, 2014, 39: 11537

[28] Grass M E, Zhang Y W, Butcher D R, Park J Y, Li Y M, Bluhm H, Bratlie K M, Zhang T F, Somorjai G A. *Angew Chem Int Ed*, 2008, 47: 8893

[29] Aliaga C, Park J Y, Yamada Y, Lee H S, Tsung C K, Yang P D, Somorjai G A. *J Phys Chem C*, 2009, 113: 6150

[30] Yoshida M, Takanabe K, Maeda K, Ishikawa A, Kubota J, Sakata Y, Ikezawa Y, Domen K. *J Phys Chem C*, 2009, 113: 10151

[31] Sakamoto N, Ohtsuka H, Ikeda T, Maeda K, Lu D L, Kanehara M, Teramura K, Teranishi T, Domen K. *Nanoscale*, 2009, 1: 106

[32] Maeda K, Teramura K, Lu D L, Saito N, Inoue Y, Domen K. *Angew Chem Int Ed*, 2006, 45: 7806

[33] Maeda K, Teramura K, Lu D L, Saito N, Inoue Y, Domen K. *J Phys Chem C*, 2007, 111: 7554

[34] Coey J M D. *Acta Crystallogr Sect B*, 1970, 26: 1876

[35] Quek X Y, Guan Y J, Hensen E J M. *Catal Today*, 2012, 183: 72

[36] Crespo-Quesada M, Andanson J M, Yarulin A, Lim B, Xia Y N, Kiwi-Minsker L. *Langmuir*, 2011, 27: 7909

[37] Maeda K, Lu D L, Teramura K, Domen K. *Energy Environ Sci*, 2010, 3: 471

[38] Maeda K, Teramura K, Lu D L, Takata T, Saito N, Inoue Y, Domen K. *J Phys Chem B*, 2006, 110: 13753

[39] Kandiel T A, Dillet R, Robben L, Bahnemann D W. *Catal Today*, 2011, 161: 196

[40] Li Y X, Lu G X, Li S B. *J Photochem Photobiol A*, 2002, 152: 219

[41] Maeda K. personal communication

[42] Hahn C, Fardy M A, Nguyen C, Natera-Comte M, Andrews S C, Yang P D. *Israel J Chem*, 2012, 52: 1111

[43] Busser G W, Mei B, Muhler M. *ChemSusChem*, 2012, 5: 2200

[44] Dionigi F, Vesborg P C K, Pedersen T, Hansen O, Dahl S, Xiong A K, Maeda K, Domen K, Chorkendorff I. *J Catal*, 2012, 292: 26

[45] Song W Y, Jansen A P J, Degirmenci V, Ligthart D A J M, Hensen E J M. *Chem Commun*, 2013, 49: 3851

[46] Grass M E, Joo S H, Zhang Y W, Somorjai G A. *J Phys Chem C*, 2009, 113: 8616

[47] Joo S H, Park J Y, Renzas J R, Butcher D R, Huang W Y, Somorjai G A. *Nano Lett*, 2010, 10: 2709

[48] Park J Y, Aliaga C, Renzas J R, Lee H, Somorjai G A. *Catal Lett*, 2009, 129: 1

[49] Shimura K, Kawai H, Yoshida T, Yoshida H. *Chem Commun*, 2011, 47: 8958

[50] Shimura K, Kawai H, Yoshida T, Yoshida H. *ACS Catal*, 2012, 2: 2126

[51] Nilekar A U, Alayoglu S, Eichhorn B, Mavrikakis M. *J Am Soc Chem*, 2010, 132: 7418